J1B.6

A MULTI-CASE STUDY OF ENSEMBLE-BASED ASSIMILATION OF RADAR OBSERVATIONS INTO CLOUD-RESOLVING WRF USING DART

Altuğ Aksoy, Chris Snyder, and David C. Dowell
National Center for Atmospheric Research †, Boulder, Colorado

1. INTRODUCTION

One of the long-standing problems in meteorology is the estimation of the three-dimensional wind and thermodynamic fields for convective-scale numerical forecasting. At this scale, Doppler radars are excellent sources of volumetric information and, naturally, much research has been focused on the retrieval of state variables from Doppler radar observations.

Several factors make the use of Doppler radar observations for convective-scale retrieval a very challenging task. First and foremost, the absence of balances like geostrophy between the wind and mass fields forces estimation schemes to rely solely on the dynamical information from the underlying numerical models, which causes the convective-scale estimation processes to be much more prone to systematic errors compared to their larger-scale counterparts. Second, Doppler radars only observe a limited subset of the state of the atmosphere through the aggregate reflectivity measurements for which numerical models have to rely on parameterizations of microphysical processes to establish relationships between "observed" moist variables and other unobserved dynamical variables. Due to large known systematic errors associated with microphysical parameterizations (Stoelinga et al. 2003), the reliability of the model-produced covariance information between such observed and unobserved variables becomes questionable. Furthermore, strong nonlinearities associated with moist variables and precipitation frequently violate the Gaussian assumptions underlying many of the estimation techniques available. Finally, in addition to instrument-related errors, Doppler radar observations contain significant representativeness errors. Although this mainly arises from the resolution mismatches commonly seen between observations and models (typical convective-scale model horizontal resolutions are still on the order of a few kilometers, while Doppler radar along-beam resolutions are on the order of a few hundred meters and across-beam distances are even smaller very near the radar), contributions to reflectivity from non-modeled sources such as birds, insects, and ground clutter also add to the complexity of the representativeness problem.

Over the past 30 years, various methods have been proposed for analyzing the convective-scale atmospheric state from Doppler radar observations. These range from purely kinematic considerations to sophisticated variational data assimilation schemes (see Dowell et al. [2004a] for a good historical discussion on such techniques). While variational techniques, and especially the better-established state-of-the-art four-dimensional variational assimilation (4DVAR), have demonstrated considerable success at estimating unobserved variables given Doppler radar observations (e.g., Sun 2005; Xiao et al. 2005; Weygandt et al. 2002; Gao et al. 1999; and Sun and Crook 1997), several factors associated with 4DVAR make its implementation to convective scales difficult. Among these, the high cost of developing and maintaining an adjoint model and the need to include in the adjoint highly nonlinear microphysical processes, the necessity to employ tractable and typically idealized models of background error covariance matrices, and the difficulty of the cost function minimization in the absence of balance constraints are especially relevant for convective scales.

Very recently, the ensemble Kalman filter (EnKF) has been proposed as an alternative data assimilation method for the assimilation of Doppler radar data using simulated observations (Snyder and Zhang 2003; Zhang et al. 2004). First proposed by Evensen (1994) for geophysical applications, the EnKF obtains the background covariance information from an ensemble of forecasts. More specifically, an ensemble of forecasts is produced at predetermined analysis intervals, available observations at which are assimilated to produce the analysis state that becomes the initial conditions for the following forecast run. This cycle is repeated sequentially in time. As a result of its sequential nature and the affordability introduced by the sampling of covariance information, the ensemble approach to data assimilation naturally brings about the advantage of employing a flow-dependent background covariance matrix Furthermore, when observation errors are uncorrelated, observations can be assimilated serially, making the EnKF algorithms very suitable for parallelization. Finally, because the filter algorithm is sequential and serial in nature, its implementation and maintenance is quite straightforward and, except the forward operator code between the model and observation spaces, is independent of the underlying forecast model.

The above-mentioned distinct differences of the EnKF in comparison to the 4DVAR make the EnKF an attractive alternative data assimilation method, as a

Corresponding Author Address: Altuğ Aksoy, The National Center for Atmospheric Research, P.O. Box 3000, Boulder, CO, 80307-3000. *E-mail:* aksoy@ucar.edu.

† The National Center for Atmospheric Research is sponsored by the National Science Foundation.

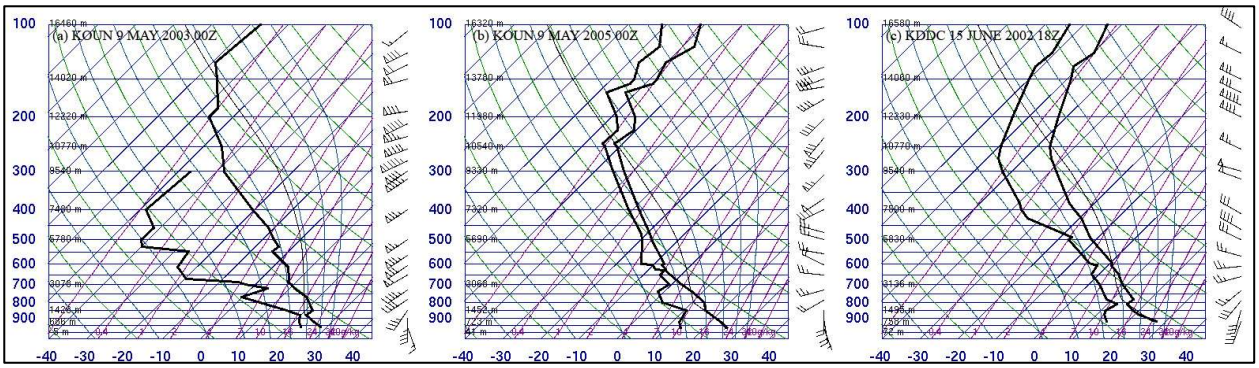

Figure 1. Skew T diagrams for the environmental soundings used for 3 cases: (a) KOUN 9 May 2003 00Z, (b) KOUN 9 May 2005 00Z, and (c) 15 June 2002 KDDC 18Z. Temperature (ºC) profiles are on the left and dew point (ºC) profiles are on the right in each panel. Horizontal wind vectors are shown at the right of each panel (half barbs 5 knots, full barbs 10 knots, flags 50 knots).

result of which, research on the EnKF has become very active in recent years, beginning with applications to global and synoptic scales. At these scales, the implementation of the EnKF has today reached near-operational status at the Canadian Meteorological Centre using data from conventional observation platforms (Houtekamer et al. 2005). At convective scales, the feasibility of the EnKF for the assimilation of Doppler radar data has been first tested by Snyder and Zhang (2003) and then by Zhang et al. (2004) using simulated radial velocity observations. Caya et al. (2005) again employed simulated Doppler radar observations to facilitate a comparison between the EnKF and the 4DVAR methods. Tong and Xue (2005) tested the EnKF using a different cloud model utilizing a six-species ice microphysics scheme and assimilating both simulated radial velocity and reflectivity observations. Meanwhile, the only real-data studies on the application of the EnKF to convective scales are Dowell et al. (2004a and 2004b), where both radial velocity and reflectivity observations are assimilated.

Previous work on ensemble-based convective-scale radar data assimilation has certain limitations. First and foremost, very limited research is carried out using real Doppler radar observations, whereas the feasibility of the EnKF is ultimately dependent upon its performance with real data where systematic model errors should play a role and could degrade results considerably. As a result, investigation of such issues as spread deficiency and model error have been very limited. Also, all of the previous work has been unanimously focused on supercell cases, generating the question of whether and how the EnKF's performance would be different in atmospheric environments that support other types of convective systems. Furthermore, use of clear-air reflectivity data has not at all been explored in the literature. Variety in how the atmospheric state is initialized is another aspect that has received limited attention across the existing body of research on ensemble-based radar data assimilation. Ensemble initialization across previous work varies from randomly perturbed soundings to randomly placed bubbles, making it difficult to compare results among them.

The present study seeks to address some of the above-mentioned shortcomings in the previous work on the EnKF for radar data assimilation in order to draw more generalized conclusions for its performance at convective scales. Our primary goal is to demonstrate the EnKF's performance across a variety of cases with different convective characteristics. We chose to use the 8 May 2003 case supercell case near Oklahoma City as a benchmark to which we can compare our results from other cases. Two other cases, a multicell case of 8 May 2005 in central Oklahoma and a bow echo case of 15 June 2002 in western Kansas accompany the 8 May 2003 supercell case. Another goal is to obtain comparable results across cases by utilizing similar overall model, ensemble, and assimilation properties. The numerical model used in this study is the Weather Research and Forecasting (WRF) model in its idealized mode. As for data assimilation, the EnKF implementation of the Data Assimilation Research Testbed (DART) is employed.

2. DESCRIPTION OF THE CASES

Several criteria have been a factor in selecting the cases for this study. While we wanted to have a set of cases representing a variety of convective behavior, nevertheless, the events we chose all occurred within the coverage of a single radar, thus allowing for relatively small computational domains. Another criterion was to initialize with soundings that represented the mature phases of respective events. The selected cases also have the common property that dense surface observations exist for the duration of the respective events (for the Oklahoma cases the data exist through the Oklahoma Mesonet, while for the Kansas case the data exist through the International H2O Project [IHOP]). In the following, each case is briefly described in terms of their synoptic environment and convective evolution.

2.1 The 8 May 2003 Oklahoma Supercell Case

The mature phase of the 8 May 2003 supercell is represented by the 9 May 00Z Oklahoma City (KOUN) sounding (Fig. 1a). The convective available potential

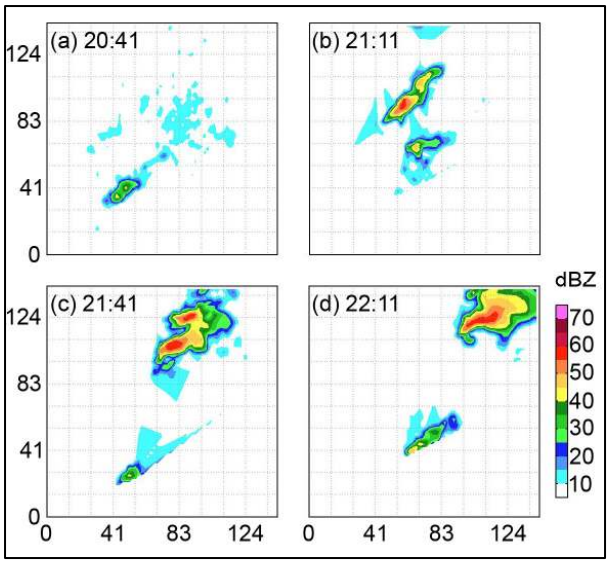

Figure 2. Evolution of the 8 May 2003 supercell storm. Contoured field shown is observed reflectivity at lowest scan angle (5 dBZ contours). The x and y axes are distance (km). Panel times are in standard UTC.

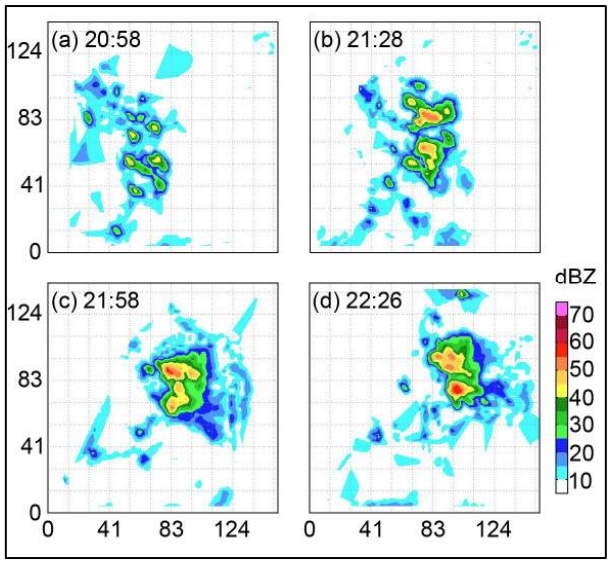

Figure 3. Evolution of the 8 May 2005 multicell system. Contoured field shown is observed reflectivity at lowest scan angle (5 dBZ contours). The x and y axes are distance (km). Panel times are in standard UTC.

energy (CAPE) associated with this sounding is 3800 J/kg, while the convective inhibition (CIN) is computed as 50 J/kg. During the afternoon of 8 May 2003, several convective cells formed along a dryline in west-central Oklahoma. Only one of these cells evolved into a tornadic supercell. During most of its life cycle, the supercell remained relatively close to the Oklahoma City radar site (KTLX). The evolution of the storm is summarized in Fig. 2. Initialization occurs at around 20:41 UTC about 40 km north of the existing convective cells (Fig. 2a). The supercell storm goes through a split starting at around 21:11 UTC (Fig. 2b) and the right mover matures into the tornadic Oklahoma City supercell near 22:11 UTC (Fig. 2d).

2.2 The 8 May 2005 Oklahoma Multicell Case

The mature phase of the 8 May 2005 multicellular system is represented by the 9 May 00Z KOUN sounding (Fig. 1b). The convective available potential energy (CAPE) associated with this sounding is 1410 J/kg, while the convective inhibition (CIN) is computed as 75 J/kg. Nevertheless, this is a very moist sounding especially in mid-troposphere, contributing to the multicellular nature of the event. During the day of 8 May 2005, numerous convective activity was observed along a dryline in central Texas and west-central Oklahoma. In afternoon hours, as a result of strong surface heating and moisture convergence, stronger convection initiated in north central Texas and south central Oklahoma. During most of its life cycle, the system remained relatively close to the KTLX radar site. The evolution of the storm is summarized in Fig. 3. Numerous convective cells form at around 20:58 UTC (Fig. 2a). Strong convection continues while the convective area merges into larger cells (Fig. 2c and 2d). Although beyond our simulation window, , the system after 23:30 UTC begins to interact with a surface boundary from earlier convection in east Oklahoma and ultimately evolves into a linear system (not shown).

2.3 The 15 June 2002 Kansas Bow Echo Case

The mature phase of the 15 June 2002 bow echo is best represented by the 15 June 18Z Dodge City, Kansas (KDDC) sounding (Fig. 1c). The convective available potential energy (CAPE) associated with this sounding is 910 J/kg, while the convective inhibition (CIN) is computed as 135 J/kg. Although not having impressive CAPE, the relatively moist profile in mid-troposphere, strong inhibition that delays initiation, and directional shear contributed to the linear nature of the event. During most of its life cycle, the system

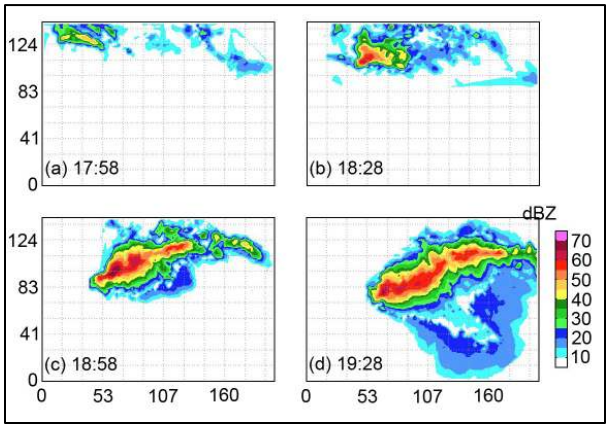

Figure 4. Evolution of the 15 June 2002 bow echo system. Contoured field shown is observed reflectivity at lowest scan angle (5 dBZ contours). The x and y axes are distance (km). Panel times are in standard UTC.

Table 1. Summary of case-specific properties of the numerical model, bubble initialization, and radar sites.

	08 May 2003 Case	08 May 2005 Case	15 June 2002 Case
WRF Model Properties			
Location of Domain Center (latitude/longitude)	34.99 N / 97.85 W	34.66 N / 97.83 W	38.26 N / 100.8 W
Domain Size (north-south/east-west, km)	150 / 150	150 / 250	150 / 210
Elevation of Model Surface (m above sea level)	388	388	1113
Time of first assimilation (UTC)	20:41	20:58	17:58
Bubble Placement Specifics			
Number of seeds	1	2	2
Number of bubbles for each seed	8	5	5
Radar Site Properties			
Name of Radar	Oklahoma City (KTLX)	Oklahoma City (KTLX)	Goodland (KGLD)
Location of Radar (latitude/longitude)	35.33 N / 97.28 W	35.33 N / 97.28 W	39.37 N / 101.70 W
Radar Location Inside or Outside of Domain?	Inside	North boundary	Outside

remained relatively close to the Goodland, Kansas (KGLD) radar site. The evolution of the storm is summarized in Fig. 4. Multiple cells initialize at around 17:58 UTC (Fig. 4a) which then begin to merge into larger cells by 18:28 UTC (Fig. 4b). The system then evolves into its final bow-echo structure between 18:58 UTC and 19:28 UTC (Fig. 4c and 4d). Later on during its life cycle, the system also produces a tornado on its southwestern edge.

3. DESCRIPTION OF THE FORECAST MODEL AND THE DATA ASSIMILATION SCHEME

3.1 The Weather Research and Forecasting (WRF) Model and Model Configuration

For the present study, the Weather Research and Forecasting (WRF) model version 2.1 is used, which is the next-generation, nonhydrostatic, community mesoscale model (Skamarock et al. 2005) using a terrain-following mass coordinate. The homogeneous idealized configuration is initialized with an environmental sounding and has open lateral boundary conditions. In this mode, there are no boundary layer or land-surface characterizations within the model. All of the experiments described in this study employ flat terrain (with model surface specified at same elevation as the respective radar site), explicit convection, and a 6-hydrometeor ice microphysics parameterization (Lin et al. 1983). While the open-lateral-boundary configuration limits the model's access to the larger-scale mesoscale environment by the initial sounding, we nevertheless believe that this is not a major disadvantage because complexities associated with initializing from a three-dimensional mesoscale environment have not at all been explored previously and thus would complicate the comparison of results among the chosen cases.

All 3 cases analyzed in this study are simulated within domains of 2-km horizontal and 500-m grid spacings. Model tops are set at 18 km for all cases. Further case-specific details are summarized in Table 1. To mimic a realistic operational setting, no attempt has been made to modify the available observed soundings.

3.2 The Data Assimilation Research Testbed (DART) and the Configuration of Data Assimilation

The Data Assimilation Research Testbed (DART) is a powerful and adaptive collection of ensemble-based data assimilation algorithms for geophysical applications parallelizable on many platforms, developed and maintained at the National Center for Atmospheric Research's (NCAR) Institute for Mathematics Applied to Geosciences (IMAGe),. In this study, we employ the parallel EnKF algorithm of DART (Anderson and Collins 2006). As a direct result of the assumption of uncorrelated observation errors, the algorithm processes available observations serially. Each update within the serial loop is equivalent to updating the elements of the state vector by a scalar observation with specified error variance. For localization, a compactly supported fifth-order correlation function following Gaspari and Cohn (1999) is employed. For all of the experiments, assimilations of radial velocity and precipitation-induced reflectivity observations are carried out using a horizontal localization radius (at which correlation weights become zero) of 5 km, while vertically, correlations are let to become zero at 4 km above/below observations. When clear-air reflectivity observations are assimilated, due to their extensive volumetric coverage, these observations are only allowed to influence their nearest respective grid points horizontally, while a 4-km vertical localization radius is still applied.

Our experiments have in general revealed a deficiency in ensemble spread that caused underfitting to the observations. To partially overcome this problem, we have applied constant covariance inflation to the prior ensemble states immediately before the start of each assimilation cycle. While inflation factors up to 1.05 have been observed to help maintain higher spread values at assimilation cycles (which improved the fit to observations), larger factors have caused violations of the model's instability criteria.

All experiments are carried out with a constant assimilation window of 2 minutes for a duration of 1 hour

(20 cycles). At each assimilation cycle, the DART algorithm looks for and assimilates only observations that are within 1 minute before and after the respective assimilation time. All such observations within this window are treated by the algorithm as if they were simultaneous. The model is advanced for 2 minutes before the next assimilation cycle is performed. Since a full volumetric scan for operational National Weather Service (NWS) WSR-88D radars takes on average about 6 minutes to complete (in storm mode), the assimilation of a complete volume scan data is carried out over 3 assimilation cycles. Finally, no quality control is applied to observations during assimilation for their expected difference from model-predicted observation values, mainly to eliminate the possibility that the commonly deficient spread would cause too many observations to be rejected.

4. ENSEMBLE INITIAL CONDITIONS

All experiments are carried out with 50 ensemble members. Two sources of uncertainty have been assumed in generating ensemble initial conditions. The first one is the uncertainty in the environmental soundings. We applied sinusoidal random perturbations to the base sounding on the 3 largest vertical modes. Sinusoidal perturbations (as opposed to purely white-noise perturbations) provide the added advantage in that they allow observations to have deeper vertical influence especially in the first few assimilation cycles when realistic covariance structures have not yet been developed by the assimilation system. Perturbations are only applied to the horizontal wind components in the base sounding similar to Dowell et al. (2004b). Our experience with perturbing the temperature and moisture fields in the sounding has been inconclusive so far, for which reason we have chosen to omit adding perturbations to temperature and moisture fields for this study. Perturbation amplitudes are 2 ms^{-1} both for zonal and meridional wind components of the base soundings.

Convective initiation in the initial field is achieved through the insertion of warm elliptical bubbles into member states. Both bubble locations and amplitudes are randomly varied to provide ensemble uncertainty. Temperature perturbations within bubbles decay exponentially from the peak amplitude until they become zero at a horizontal (vertical) radius of 8 km (1.5 km). Bubble amplitudes are drawn from a Gaussian distribution of 5-K mean and 1-K standard deviation. Amplitude values are thresholded at 2.5 K and 7.5 K. Similar to Dowell et al. (2004a and 2004b), bubble locations are limited to areas near initial convection observed in each of the cases. Depending on the location and the aerial coverage of initial convection, we define (subjectively) one or more "seed" locations, around each of which random bubbles are placed with their horizontal distance to seed locations drawn from a Gaussian distribution. We observed that this method of bubble placement, compared to equal likelihood of bubble locations within a specified area, has in general produced more coherent initial covariance structures and improved the analyses within the first few assimilation cycles. The standard deviation of the bubble distance to the seeds is set at 20 km. Similar to Tong and Xue (2005), no bubbles are placed within a horizontal distance equal to bubble radius from the lateral boundaries of the computational domain. Vertically, bubbles are placed randomly within the first 6 model levels.

To obtain more coherent covariance structures and to spin up convection in the computational domain, a 10-minute free ensemble forecast is performed from the initial bubble-state for each case and the first assimilation is carried out based on this 10-minute forecast state. Further case-specific details of bubble placement are summarized in Table 1.

5. RADAR DATA, ITS PREPROCESSING, AND ASSIMILATION

Single Doppler observations are provided by the KTLX (8 May 2003 and 8 May 2005 cases) and KGLD (15 June 2002 case) radars. For all cases, one-hourly observations (13 full volume scans) are assimilated at 2-minute intervals. In all 3 cases, the radars operated in storm mode, producing sweeps at 14 scan angles and completing each full volume in about 6 minutes. Because of this and also depending on the distance of respective convective activity to radar location, observations at varying vertical levels and with varying numbers are assimilated in subsequent assimilation cycles.

The original data obtained from respective radars is in raw WSR-88D level II format. Preprocessing of the raw data mainly involves a Cressman-type objective analysis (Dowell et al. 2004a), local velocity unfolding, and thresholding for distance to radar and reflectivity. No vertical interpolation of the data is carried out. The resulting preprocessed observations still lie on their respective original sweep surfaces, but are interpolated horizontally to a 2-km flat grid. Owing to the canonical distribution of the objectively analyzed observations, observation locations do not coincide with the WRF's horizontal grid (produced through a Lambert map projection) and the equally-spaced vertical grid. Nevertheless, as a result of the averaging of observations at the same horizontal resolution as the model, resolution-dependent representativeness errors are believed to be minimized.

The raw WSR-88D observations include aliased velocities that must be accounted for during the observation preprocessing and assimilation procedures. First, a local unfolding technique (Miller et al. 1986) is applied during the objective analysis of raw Doppler velocity observations. Then, the objectively analyzed observations are de-aliased during the assimilation procedure by choosing the unfolding factor that produces the best agreement between the observation and the prior ensemble mean. We have had great success with this automatic de-aliasing procedure for all storm cases attempted to date.

Contamination of reflectivity data by non-precipitation sources such as birds and insects is a significant source of representativeness error and

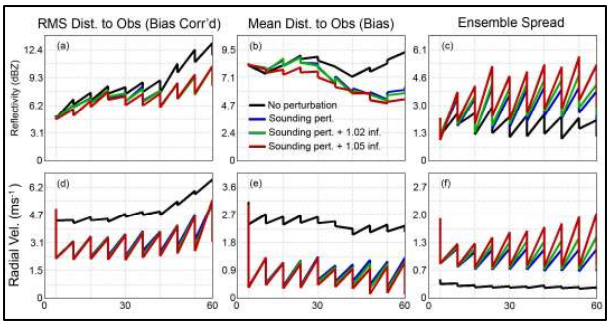

Figure 5. 60-minute evolution of prior and posterior (sawtooth shape) rms distance to observations (left panels), mean distance to observations (middle panels), and ensemble spread (right panels) for the benchmark 8 May 2003 case. Statistics are plotted for the two observed variables reflectivity (top row) and radial velocity (bottom row). Experiments shown are no sounding perturbations (black), only sounding perturbations (blue), sounding perturbations plus covariance inflation of 1.02 (green), and sounding perturbations plus covariance inflation of 1.05 (red).

manifests itself mostly as low-valued observations. To minimize the occurrence of such contamination, further preprocessing is applied to reflectivity data to omit observations of values lower than 5 dBZ. Similarly, to eliminate ground clutter which mostly occurs near the radar site, we simply chose to omit all observations within a radius of 10 km from the radar location.

In some of our experiments, we also assimilate clear-air reflectivity observations. There are two sources of clear-air reflectivity observations. The main source is the reflectivity observations that are omitted through the 5-dBZ thresholding during the preprocessing. All of such reflectivity observations become flagged "clear air" and a constant observation value of -10 dBZ is assigned to them. Another source is the grid points that are omitted by the interpolation algorithm when insufficient numbers of data points exist to perform the interpolation. Like precipitation reflectivity observations, clear-air observations are also subjected to the interpolation. Nevertheless, due to the large volume of such observations, a full volume scan on average contains about 3-4 times as many clear-air observations than precipitation observations.

Quantification of the magnitude of the observational error variance is difficult for radial velocity and reflectivity observations. We chose to use 2 ms^{-1} and 2 dBZ for the standard deviation of radial velocity and reflectivity observations, respectively. While these values are relatively small compared to other values used in the literature, we nevertheless believe that they are adequate in terms of their impact they have on the analysis states, considering the somewhat deficient ensemble spread values that were commonly observed in our experiments.

6. RESULTS

6.1 The Benchmark Case of 8 May 2003 – Investigation of Spread Deficiency

Our benchmark case of 8 May 2003 is very suitable for the investigation of the common problem of spread deficiency in convective-scale data assimilation. Although the sounding for this case has a strong CAPE, the combination of dry mid-levels and low-level inversion leads to the difficulty in the model's initiation and maintaining of convection from warm bubbles. Figure 5 summarizes the time evolution of domain-averaged root-mean-square (rms) error, bias, and ensemble spread (standard deviation) statistics for various experiments we performed. Here and elsewhere in the manuscript, rms error, bias, and spread statistics are computed in the observation space by subtracting model-predicted observations from actual observations. In other words, bias is the mean distance of the model to the observations at each time and rms error is the mean random variation of the model about the observations. To minimize the effect of systematic differences between the model and observations, we subtract the bias from the model-observation difference before we compute the rms error.

The statistics from the control experiment with only random bubbles in the initial ensemble are shown with black lines in Figure 5. For an ideal ensemble, the expected distance between the model and observations should, on average, correspond to the square-root of the sum of the variances of observational and forecast uncertainties. We see that for both reflectivity and radial velocity observations, the spread becomes steadily smaller: By the end of the 60-minute experiment, the forecast spread is only about 5% of its expected value for both observed variables. This deficiency clearly leads to underfitting of observations as demonstrated by the high level of overall forecast error (distance to observations, estimated by the sum of absolute bias and rms error), which is at 22 dBZ (9 ms^{-1}) for reflectivity (radial velocity) at the 60-minute cycle.

Several factors can lead to deficient forecast spread. Not including a realistic environmental uncertainty in the initial ensemble is possibly one of the major contributors to the deficiency of spread. To address this issue, we introduced sinusoidal perturbations to the base state in the vertical. The results from the experiment with 2 ms^{-1} wind perturbation magnitude and the same bubble locations and magnitudes as the control experiment are summarized by the blue lines in Figure 5. Two other potential sources for spread deficiency are more difficult to account for. While sampling error due to the limited ensemble size does lead to underestimation of forecast uncertainty, unaccounted model error can also cause large differences between the model and observations. One simple way to address these two latter issues is the application of covariance inflation prior to assimilating observations. Two additional experiments with constant prior state-space covariance inflation of 1.02 (1.05) (in addition to bubbles and sounding perturbation) are

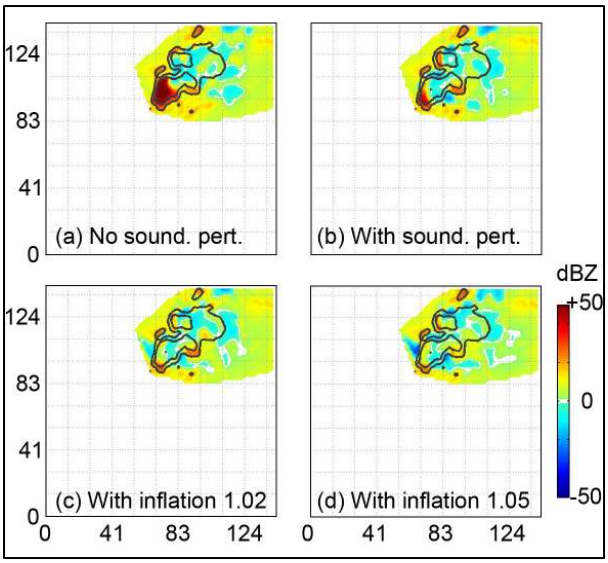

Figure 6. 60-minute observation-forecast difference for reflectivity (contoured at 1 dBZ) at the lowest scan angle for the benchmark 8 May 2003 case. Experiments shown are (a) no sounding perturbations, (b) only sounding perturbations, (c) sounding perturbations plus covariance inflation of 1.02, and (d) sounding perturbations plus covariance inflation of 1.05. For comparison, the observation values at the same time are outlined at 20 dBZ and 40 dBZ with black counturs.

shown with green (red) lines. From sounding-perturbation-only experiment to the 1.05-inflation-factor experiment, we see a progressive improvement in the level of overall spread in the ensemble for both observed variables (Figure 5c and f). Because the sounding perturbations are in the wind fields, improvement in the spread of radial velocity is much more pronounced. As a direct result of increased ensemble spread, and as a sign of improved fitting to observations, bias values also drop considerably. Finally, the overall forecast error at the 60-minute cycle is reduced by 6.5 dBZ and 2 ms^{-1} for the two observed variables. Nevertheless, despite the improved levels of spread, spread deficiency is still present. At the 60-minute cycle, the forecast spread for reflectivity (radial velocity) is roughly 50% (60%) deficient for the same experiment.

Figure 6 compares the distribution of 60-minute reflectivity forecast-observation differences for the four experiments discussed. We see that, from the experiment initialized with bubbles only (Figure 6a) to the experiment with perturbed soundings and the inflation factor of 1.05 (Figure 6d), there is a significant improvement in the estimated structure especially of the main storm. The most striking improvement occurs in the main updraft region, which appears to be entirely missed in Figure 6a. Progressively, errors in the main updraft and outflow regions of the primary storm and its left mover are reduced and most errors are confined to a narrow band in the periphery of the main storm. Meanwhile, errors outside the main storm system are changed very little across the experiments, mainly due to the insufficient spread found in those locations (spread distribution not shown for brevity).

6.2 8 May 2005 and 15 June 2002 Cases – Investigation of the Impacts of Clear-Air Reflectivity Data

When we applied the optimal settings obtained from the 8 May 2003 benchmark case, namely initial conditions with bubbles and sounding perturbations and a covariance inflation factor of 1.05, to the 8 May 2005 and 15 June 2002 cases, we encountered another problem that we believe is generic to some convective situations. The problem arises from initializing with an environmental sounding that the forecast model favors for convection. In such a case, convection is initiated at many of the randomly placed bubble locations in ensemble members, and a wide-spread convective area forms in the mean state. When one assimilates only reflectivity data obtained from the observed precipitation region, it is impossible for the assimilation system to suppress such spurious convection at typical localization radii (see also Snyder and Zhang 2003). The formation and the evolution of such spurious convective activity is shown for the 8 May 2005 and 15 June 2002 cases in Figure 7. In the experiment shown, reflectivity data assimilated comes from the respective observed precipitation regions only (through our thresholding of reflectivity observations at 5 dBZ during preprocessing). For comparison, observed 30-dBZ regions are highlighted by black contour lines. We see that while the assimilation system actually captures the structure of the observed convective activity relatively well, many spurious cells outside the observed precipitation region form, expand, and propagate, deteriorating the quality of the analysis considerably.

As a remedy to the problem of spurious cell formation, we assimilated clear-air reflectivity data in addition to precipitation reflectivity and radial velocity observations used thus far in the experiments. The corresponding analyses from this experiment are shown at the same times and for the same cases in Figure 8. We see that considerable suppression of precipitation occurs early during the experiment and progressively better analyses of the actual precipitating system are obtained as more data is assimilated over time. While the suppression of spurious cells in analysis states is in itself an improvement of the assimilation system, we also analyze the impacts of assimilating clear-air reflectivity data through statistics computed within the precipitation region itself. Since identical precipitation-reflectivity observations are assimilated in experiments with and without clear-air reflectivity data, this is a fair comparison and points to the indirect effects of clear-air data on the analysis of the respective observed convective systems. Such indirect effects can be expected to arise dynamically within the main convective system when interactions with the surrounding spurious convection are suppressed, and also through the indirect impact of vertical localization (in the horizontal direction, clear-air observations are only allowed to impact the nearest model grid point).

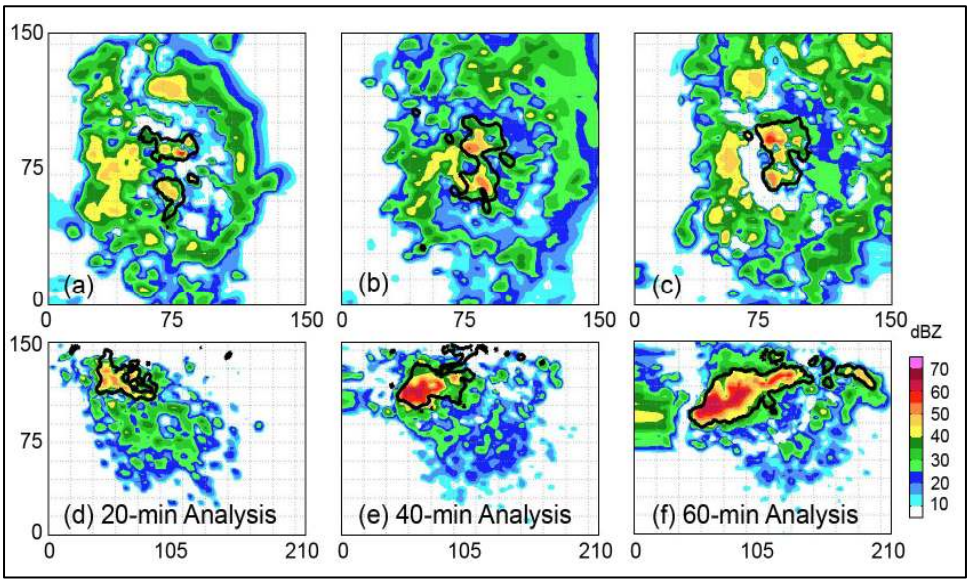

Figure 7. 20-minute (panels a, d), 40-minute (panels b, e), and 60-minute (panels c, f) analysis of reflectivity (5 dBZ contours) at 5 km for 8 May 2005 case (top rows) and 15 June 2002 case (bottom rows) without the assimilation of clear-air data. The 30-dBZ contour of observed reflectivity at corresponding height and time is shown with solid black lines for comparison. The x and y axes are distance in km.

The rms error, bias, and spread statistics for precipitation reflectivity are summarized in Figure 9 for all 3 cases investigated in this study. Noticeable improvement is achieved in the bias statistics between experiments without and with clear-air reflectivity data (compare red dashed lines to green dashed lines). The improvement is most pronounced for the 8 May 2003 cases, where the difference on average is between 3-5 dBZ, while the smallest improvement occurs for the 15 June 2002 case. But even for this case, the reduction in bias is about 1 dBZ at 30 minutes. Figure 9 also reveals that the reduction in bias is somewhat compensated by an increase in the rms error statistics from the experiments without to the experiments with the clear-air data (compare red solid lines to green solid lines). However, for all cases and at all times, the magnitude of

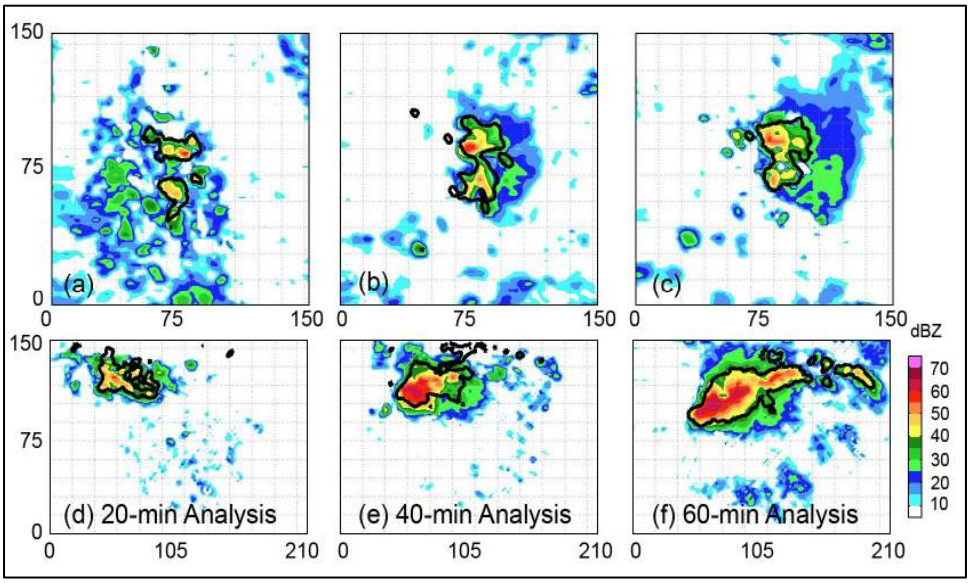

Figure 8. 20-minute (panels a, d), 40-minute (panels b, e), and 60-minute (panels c, f) analysis of reflectivity (5 dBZ contours) at 5 km for 8 May 2005 case (top rows) and 15 June 2002 case (bottom rows) with the assimilation of clear-air data. The 30-dBZ contour of observed reflectivity at corresponding height and time is shown with solid black lines for comparison. The x and y axes are distance in km.

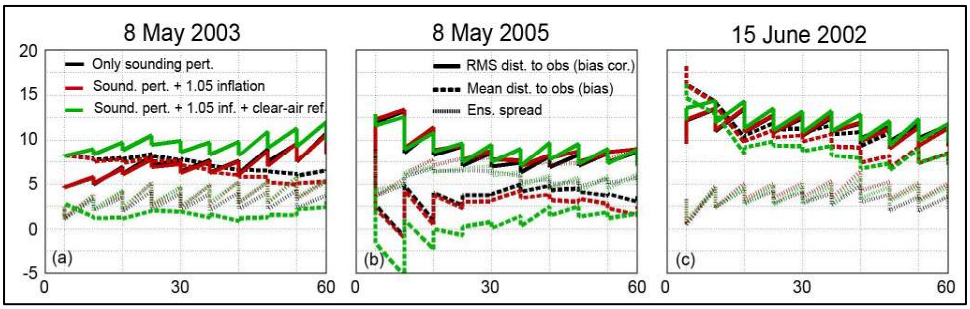

Figure 9. Time evolution of rms error (solid), bias (dashed), and ensemble spread (dotted) for the (a) 8 May 2003, (b) 8 May 2005, and (c) 15 June 2002 cases for observed precipitation reflectivity. Experiments shown are only sounding perturbations (black, no clear-air data assimilated), sounding perturbations and 1.05 inflation factor without (red) and with (green) the assimilation of clear-air reflectivity data. The y axis units are dBZ and the x axis units are minutes.

the increase in rms error remains less than the magnitude of the decrease in bias, so that the level of overall error nevertheless is reduced.

The simultaneous decrease in bias and increase in rms error is possible because while the bias arises from broad areas of systematic observation-forecast differences, rms error is associated with localized narrow peaks of observation-forecast differences. We observe that clear-air observations lead to the reduction of bias in such broad features but do not have much impact on the magnitudes of narrow observation-model difference peaks. Consequently, while bias is reduced, relative distance of the model to observations in such narrow peaks increases, leading to an increase in rms error.

7. CONCLUSIONS AND PLAN FOR FUTURE WORK

More vigorous research is needed on how best to initialize an ensemble and maintain spread throughout the cycling of observations. The large observed impact of initialization with perturbed soundings hints at the need to force the model with realistic mesoscale uncertainty. Meanwhile, due to the large volume of radar data observations, repeated cycling of observations also imposes a challenge on maintaining sufficient levels of ensemble spread. While we have demonstrated that covariance inflation can help maintain higher levels of spread, methods that selectively introduce additive noise to regions of observed precipitation will likely be more effective in introducing more realistic perturbations to the model state. In the future, we are planning on expanding our research to investigate one such technique that we are implementing to the WRF-DART system. Finally, sensitivity of analysis quality to initial conditions is another aspect we are considering to examine in the future.

We are also planning to expand our investigation to storm-scale forecasting for each case based on 60-minute analysis states obtained through various experimental settings. Clearly, this is a much more challenging problem and it is not obvious how relative impacts to the analyses by different techniques such as perturbed soundings, inflation, and assimilation of clear-air data will translate to differences in the quality of forecasts.

8. REFERENCES

Anderson, J.L. and N. Collins, 2006: Scalable implementations of ensemble filter algorithms for data assimilation. To appear in *J. Atmos. Ocean. Tech. – A*.

Caya, A., J. Sun, and C. Snyder, 2005: A Comparison between the 4DVAR and the Ensemble Kalman Filter Techniques for Radar Data Assimilation. *Mon. Wea. Rev.*, **133**, 3081-3094.

Dowell, D.C., F. Zhang, L.J. Wicker, C. Snyder, and N.A. Crook, 2004a: Wind and temperature retrievals in the 17 May 1981 Arcadia, Oklahoma, supercell: Ensemble Kalman filter experiments. *Mon. Wea. Rev.*, **132**, 1982-2005.

Dowell, D.C., L.J. Wicker, and D.J. Stensrud, 2004b: High resolution analyses of the 8 May 2003 Oklahoma City storm. Part II: EnKF data assimilation and forecast experiments. Preprints, *22nd Conf. Severe Local Storms*, Hyannis, MA, Amer. Meteor. Soc.

Evensen, G., 1994: Sequential data assimilation with a nonlinear quasi-geostrophic model using Monte Carlo methods to forecast error statistics. *J. Geophys. Res.*, 99 (C5), 10143-10162.

Gao, J.-D., M. Xue, A. Shapiro, and K.K. Droegemeier, 1999: A variational method for the analysis of three-dimensional wind fields from two Doppler radars. *Mon. Wea. Rev.*, **127**, 2128-2142.

Gaspari, G. and S.E. Cohn, 1999: Construction of correlation functions in two and three dimensions. *Quart. J. Roy. Meteor. Soc.*, **125**, 723-757.

Houtekamer, P. L., L. M. Herschel, G. Pellerin, M. Buehner, M. Charron, L. Spacek, and B. Hansen (2005), Atmospheric data assimilation with an ensemble Kalman filter: Results with real observations. *Mon. Wea. Rev.*, **133**, 604-620.

Lin, Y.-L., R.D. Farley, and H.D. Orville, 1983: Bulk parameterization of the snow field in a cloud model. *J. Climate Appl. Meteor.*, **22**, 1065–1092.

Miller, L.J., C.G. Mohr, and A.J. Weinheimer, 1986: The simple rectification to Cartesian space of folded radial velocities from Doppler radar sampling. *J. Atmos. Oceanic Technol.*, **3**, 162-174.

Skamarock, W.C. , J.B. Klemp, J. Dudhia, D.O. Gill, D.M. Barker, W. Wang, J.G. Powers, 2005: A description of the Advanced Research WRF version 2. *NCAR Tech. Note* NCAR/TN-468+STR, 88 pp.

Snyder, C. and F. Zhang, 2003: Assimilation of simulated Doppler radar observations with an ensemble Kalman filter. *Mon. Wea. Rev.*, **131**, 1663-1677.

Stoelinga, M.T., P.V. Hobbs, C.F. Mass, and co-authors, 2003: Improvement of microphysical parameterization through observational verification experiment. *Bull. Amer. Meteor. Soc.*, **84**, 1807-1826.

Sun, J., 2005: Initialization and numerical forecasting of a supercell storm observed during STEPS. *Mon. Wea. Rev.*, **133**, 793-813.

Sun, J. and N.A. Crook, 1997: Dynamical and microphysical retrieval from Doppler radar observations using a cloud model and its adjoint. Part II: Retrieval experiments of an observed Florida convective storm. *J. Atmos. Sci.*, **55**, 835-852.

Tong, M. and M. Xue, 2005: Ensemble Kalman filter assimilation of Doppler radar data with a compressible nonhydrostatic model: OSS experiments. *Mon. Wea. Rev.*, **133**, 1789-1807.

Weygandt, S.S., A. Shapiro, and K.K. Droegemeier, 2002: Retrieval of model initial fields from single-Doppler observations of a supercell thunderstorm. Part II: Thermodynamic retrieval and numerical prediction. *Mon. Wea. Rev.*, **130**, 454-476.

Xiao, Q., Y.-H. Kuo, J. Sun, W.-C. Lee, E. Lim, Y.-R. Guo, and D.M. Barker, 2005: Assimilation of Doppler radar observations with a regional 3DVAR system: Impact of Doppler velocities on forecasts of a heavy rainfall case. *J. Appl. Meteor.*, **44**, 768–788.

Zhang, F., C. Snyder, and J. Sun, 2004: Impacts of initial estimate and observation availability on convective-scale data assimilation with an ensemble Kalman filter. *Mon. Wea. Rev.*, **132**, 1238-1253.